# Ultra-Wideband Channel Model for Intra-Vehicular Wireless Sensor Networks

**A thesis submitted in fulfilment of the requirements**
**for the degree of Master of Science in Engineering**
**Koc University, 2012**


**C.Umit Bas**

Graduate School of Science and Engineering
Koc University
Turkey

**Koc University**

**Graduate School of Science and Engineering**

**June 2012**

**This is to certify that I have examined this copy of master's thesis by**

## C.Ümit Baş

**and have found it is complete and satisfactory in all respects, and that are all revisions required by the final examining committee have been made.**

**Committee:**

---

Asst. Prof. Sinem Çöleri Ergen (Advisor)

---

Assoc. Prof. Öznur Özkasap

---

Prof. Murat Tekalp

*Her zaman yanımda olan*

*Ailem'e*

# Acknowledgements

I would like to express my sincere gratitude and profound respect to my Advisor Assist. Prof. Sinem Çöleri Ergen for his reliable guidance, inspiration and valuable support. I am also grateful to members of my thesis committee Prof. Murat Tekalp and Assoc. Prof. Öznur Özkasap for their valuable comments and serving on my defense committee.

First and foremost, I am really thankful to my beloved İrem. In addition to her support and love, she gave me new dreams and the courage to realize them. Next I would like to thank Yalçın, it has been a pleasure sharing our home, our office and our time with you for years. Also I would like to thank Tolga who is my first friend at Koç and answered countless questions of mine from then. Gratitudes to all of my friends who make my time in Koç unforgettable: Burak, Şebnem, Duygu, Pelin, Remziye, Şaziye, Meltem, Nihan, Merve E., Merve G., Bekir, Berk and Hilmi.

Finally I would like to thank my parents and my sister, for their faith and unlimited support to me. Without their help and support, there would be none of this; therefore I dedicate this work to them.

# Abstract

Intra-vehicular wireless sensor networks is a promising new research area that can provide part cost, assembly, maintenance savings and fuel efficiency through the elimination of the wires, and enable new sensor technologies to be integrated into vehicles, which would otherwise be impossible using wired means, such as Intelligent Tire. The most suitable technology that can meet high reliability, strict energy efficiency and robustness requirements of these sensors in such harsh environment at short distance is Ultra-Wideband (UWB). However, there are currently no detailed models describing the UWB channel for intra-vehicular wireless sensor networks making it difficult to design a suitable communication system. We analyze the small-scale and large-scale statistics of the UWB channel beneath the chassis of a vehicle by collecting data at various locations with 81 measurement points per transmitter-receiver pair for different types of vehicles including the scenarios of turning the engine on and movement on the road. Collecting multiple measurements allows us to both improve the accuracy of the large-scale fading representation and model small-scale fading characteristics. The distance dependent path loss exponent around the tires and other locations beneath the chassis are found to be very different requiring separate models. The power variation around the

path loss has lognormal distribution. The clustering phenomenon observed in the averaged power delay profile is well characterized by Saleh-Valenzuela model. The cluster amplitude and decay rate is formulated as a function of the cluster arrival times using dual slope linear model. Such a model has not been developed before for in-vehicle environment. Cluster inter-arrival times are modeled using Weibull distribution providing a better fit than the commonly used exponential distribution in the literature mainly due to the non-randomness of the local structure of the vehicle. The variations of local power delay profiles around the small-scale averaged power delay profiles in decibels at each delay bin is modeled by Gaussian distribution with variance independent of the value of the delay and distance between transmitter and receiver. This is the first work to model small-scale channel characteristics within the vehicle. The analysis of the model parameters for different vehicles and different scenarios demonstrates the robustness of our modeling approach exhibiting small variance in channel parameters for different vehicle types. Finally, the algorithm for generating the channel model is given. The generated power delay profiles are in good agreement with the experimental ones validating our model.

# Özetçe

Araç içi sensör ağları sağladığı parça, montaj ve onarım maliyetlerindeki düşüş, kabloların çıkarılması sayesinde daha iyi yakıt etkinliği ve Akıllı Lastik gibi kablolu sensörler ile uygulanması mümkün olmayan yeni teknolojilere imkan sağlaması ile ümit vaat eden bir araştırma alanıdır. Kablosuz iletişim için böylesine zorlu bir ortamda, dayanıklılık, enerji etkinliği ve yüksek güvenilirlik gibi gereklilikleri kısa mesafeler için karşılamaya en uygun iletişim teknolojisi ultra geniş bantlı iletişimdir. Ancak araç içi kablosuz sensör ağları için uygun bir ultra geniş bant kanalını detaylı olarak tanımlayan bir kanal modeli bulunmaması uygun iletişim sistemlerinin tasarlanmasını zorlaştırmaktadır. Literatürdeki bu boşluğu doldurmak için, araç şasi altı ultra geniş bant kanalların küçük ve büyük ölçekli istatistiklerini analiz ettik. Analizlerimizde kullanmak üzere araç şasi altı ortamında, 18 farklı pozisyonda 81'er alıcı-verici çiftiyle ölçüm aldık. Her pozisyonda çoklu ölçüm almamız büyük ölçekli sönümlenme modelimizin daha tutarlı olmasını sağlamasının yanında küçük ölçekli sönümlenme niteliklerinin türetilmesine de imkan verdi. Mesafeye bağlı yol kaybı modeli, tekerleklerin etrafında şasinin altındaki diğer pozisyonlardan çok farklı olduğu tespit edildi. Güçlerin yol kaybı modelinin etrafındaki sapmalarını lognormal dağılım ile modelledik . Ortalama güç

gecikme profillerinde gözlemlenen kümelenmeleri Saleh-Valenzuela modeline uygun olduğu belirlendi. Küme büyüklükleri ve azalma oranları kümelerin geliş zamanına bağlı parçalı tanımlı doğrusal fonksiyonlar ile tanımlandı. İki ardışık küme arası geçen sürenin daha önceki modellerde kullanlan üssel dağılımın aksine, Weibull dağılım ile daha iyi bir uyum sağlamaktadır. Yerel güç gecikme profillerinin küçük ölçekli ortalaması alınmış güç gecikme profillerinin etrafındaki dağılımı, her bir gecikme aralığı için normal dağılım ile modellendi. Bu çalışma araç içinde küçük ölçekli kanal istatistiklerini inceleyen ilk çalışmadır. Farklı senaryolarda ve farklı araçlarla tekrarlanmış ölçümlerde bulunan değerlerin tutarlı olması sağlıklı bir model önerdiğimizin ispatıdır. Son olarak, kanal modelinin simülasyonlarda kullanılabilmesini sağlamak amacıyla, kanal modelinin tekrar yaratılmasını anlatan algoritma sunulmaktadır. Simülasyonlardaki ve deneysel ölçümlerdeki güç gecikme profillerinin benzerliği modelimizin geçerliliğini gözler önüne sermektedir.

# Contents

# List of Figures

# List of Tables

# Chapter 1

# Introduction

## 1.1 Intra-Vehicular Wireless Sensor Networks

The exponential increase in the number and sophistication of electronic systems in vehicles as they are replacing those that are purely mechanical or hydraulic arises the need for more sensors to monitor various quantities inside them [1]. In the current vehicle architecture, each sensor is wired to an electronic control unit (ECU), which samples and processes the information from that particular sensor. The ECUs then communicate with each other over a backbone network to share this information. Besides, the ECUs are connected to the battery of the vehicle to supply power for both their own operation and the operation of the sensors connected to them. A present day wiring harness may have up to $4,000$ parts, weigh as much as 40kg and contain up to 4km of wiring. Eliminating the wires can potentially provide

part cost, assembly and maintenance savings while also offering fuel efficiency and an open architecture to accommodate new sensors.

The full adoption of a wireless sensor network within the vehicle may not be feasible in the near future since the experience on wireless sensor networks within the vehicle is not mature enough to provide the same performance and reliability as the wired communication that has been tested for a long time with vehicles on the road. Wireless sensor networks is therefore expected to be deployed in the vehicle through either new sensor technologies that are not currently implemented due to technical limitations such as Intelligent Tire that provides high rate acceleration data from the wireless sensors embedded within the tire to improve significantly active safety control systems [2] and some sensor technologies for non-critical vehicle applications either requiring a lot of cabling such as park sensors or not functioning well enough due to cabling such as steering wheel angle sensors. Once the robustness of these wireless applications are proven, within the vehicle, it will be possible to remove the cables between the existing sensors and ECUs serving more critical vehicle applications such as an ABS (Anti-lock Braking System) system using wireless sensor network for the transmission of automotive speed data from four wheel speed sensors to the ECU [3].

## 1.2 Ultra-Wideband

Investigation of different modulation strategies including RFID [4], narrow-band [5, 6], spread spectrum [7, 8] and ultra-wideband (UWB) [9, 10, 11] for Intra-Vehicular Wireless Sensor Networks (IVWSN) in the literature demons-

trated that UWB is the most suitable technology satisfying high reliability requirement of vehicle control systems and strict energy efficiency requirement of the sensor nodes at short distance and low cost in such harsh environment containing a large number of metal reflectors, extreme temperatures and a lot of vibrations.

UWB is often defined to be a transmission from an antenna for which the emitted signal bandwidth exceeds the lesser of 500MHz and 20% of the center frequency. This large bandwidth provides resistance to multi-path fading, power loss due to the lack of line-of-sight and intentional/ unintentional interference therefore achieves robust performance at high data rate and very low transmit power. The comparison of the power spectral density of UWB systems and a narrowband system is shown in Fig. 1.1.

Historically UWB is the first of any kind of wireless communication systems, with the invention of Marconi Spark Gap Emitter in 1895 [12]. The instantaneous bandwidth of the spark gap was many times greater than the required one for their data rate. However UWB technology of the time did not provide any practical implementation since it was not able to meet the most important requirements of wireless communications such as multiple users in the same environment and methods to enable a particular user recover corresponding data stream. As a result, UWB was not used commercially and only considered for experimental work until the end of 1990s. In 1993 Robert Scholtz, professor in University of Southern California, proposed a multiple access scheme for UWB which enable UWB to support wireless networks in addition to the radar applications and point to point communications. This work sets off many investigations on the UWB propagations in the 1990s

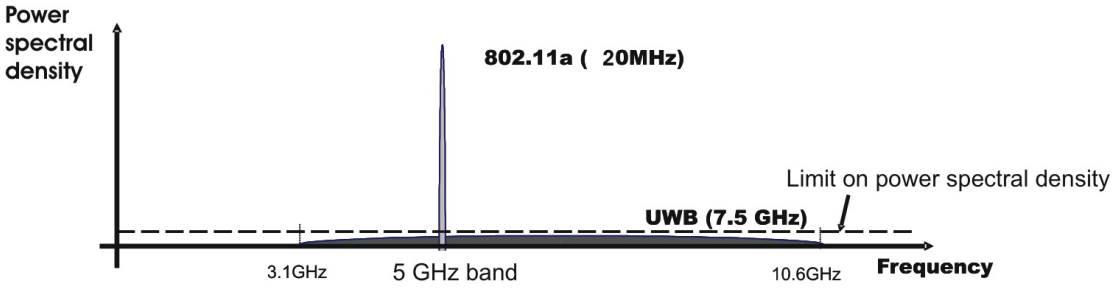


**Figure 1.1:** Comparison of Narrowband and Ultra-Wideband Systems Power Spectral Density

and 2000s, and resulted in a large number of papers about indoor/outdoor UWB propagation, characterization of the response of materials to UWB impulses, characterization of the antenna response and coexistence of UWB and narrowband systems. These studies proved merits of the UWB over narrowband system for harsh environments however they also revealed the difference in the UWB channel characteristics for different environments. Hence, we strongly believe that to enable the use of UWB for intra-vehicular wireless sensor networks, first we need to characterize create an accurate channel model.

## 1.3 Related Work

Before designing a UWB communication system, the appropriate channel model has to be extracted for the in-vehicle environment. Most UWB channel measurement campaigns have been performed in such locations as indoor [13, 14, 15, 16, 17], outdoor [18, 19, 20, 21], around the human body [22, 23] or industrial environments [24]. IEEE 802.15.3a and IEEE 802.15.4a channel modeling subgroups developed UWB channel models for high-rate and low-rate applications respectively [25, 26]. The vehicular environment however is very different from these environments due to short distances, dense multipath and lack of line of sight from most sensors to the corresponding ECU.

Building a detailed model for IVWSN requires both *classifying the vehicle* into different parts of similar propagation characteristics and *collecting multiple measurements* at various locations belonging to the same class. As shown in Fig. 1.2, the classes of similar propagation characteristics are expected

to include passenger compartment, beneath the chassis, within the engine compartment, side of the vehicle, which may be further divided into subclasses based on channel measurement results. Fig. 1.1 lists the literature on UWB channel models for different parts of the vehicle.

The channel modeling efforts in intra-vehicle environments on the other hand either concentrate on passenger compartment [27, 28, 29, 30] or the trunk [31], which is not the typical place where vehicle sensors are located, or provide measurement results for a limited sensor locations beneath the chassis or within the engine compartment [9, 10, 11], which is not enough to provide a detailed model for intra-vehicular sensors.

Although it has been stated in the overview papers on UWB channel measurements in [32, 33] that at least 50 measurement points per area are required to determine small-scale fading and all the UWB channel measurement campaigns for other applications including indoor [13, 14, 15, 16, 17], outdoor [18, 19, 20, 21], around the human body [22, 23] or industrial environments [24] model small-scale fading, it is interesting that none of the previous UWB channel measurements aim to model small-scale fading: Small-scale fading is defined as the changes in power delay profile caused by small changes in transmitter and receiver position while environment around them does not change significantly in contrast to large-scale fading that models the changes in received signal when the position of the transmitter or receiver varies over a significant fraction of distance between them and/or environment around them changes. Therefore, for a certain transmitter-receiver pair, multiple measurements separated far enough from each other while keeping the environment around them the same need to be collected generating independent

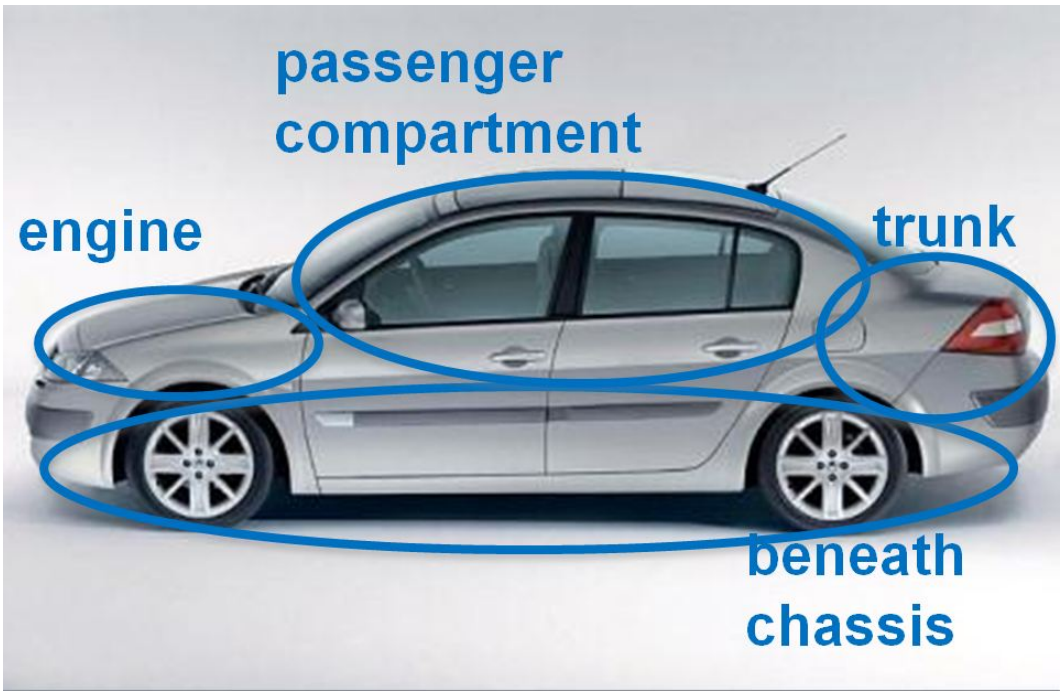


**Figure 1.2:** Groups of locations with similar propogation characteristics

measurements to both improve the accuracy of large scale fading representation and allow modeling small scale fading characteristics. Although [30] and [31] claim to provide small-scale fading characteristics, they do not use the large number of measurements to obtain a more accurate characterization of large-scale fading and model the small-scale variations around this large-scale representation.

| Reference | Measurement Location | Small-Scale | # points for Large-scale Model | Scenarios |
|---|---|---|---|---|
| [27] | passenger compartment | No | 12 | stationary, vary # passengers |
| [28] | passenger compartment | No | 3 | stationary |
| [29] | passenger compartment | No | 10 | stationary, moving |
| [30] | passenger compartment | No | 24 | stationary, vary # passengers |
| [31] | trunk | No | $17 \times 14$ | stationary, vary driver's presence |
| [9] | beneath chassis | No | 10 | stationary |
| [10] | beneath chassis | No | 10 | stationary, two types of vehicles |
| [11] | beneath chassis | No | 10 | stationary, moving |
| [9] | within engine compartment | No | 5 | stationary |
| [10] | within engine compartment | No | 9 | stationary, two types of vehicles |

**Table 1.1:** Summary of literature on intra-vehicle UWB channel measurements

## 1.4 Original Contributions

The goal of this thesis is to provide the UWB channel model for IVWSN beneath the chassis by collecting data at $18 \times 81$ measurement locations from two types of vehicles considering the scenarios of stopping vehicle with engine-off, stopping vehicle with engine-on and moving vehicle determining both large-scale and small-scale statistics. The original contributions of this thesis are four:

- We develop an accurate representation of the large-scale fading characteristics by averaging the power delay profile of 81 measurement points for each transmitter-receiver pair in contrast to the previous work that considers only 1 measurement point without removing small-scale fading effects. We derive the parameters of the path loss, power variation around mean path loss and Saleh-Valenzuela (SV) model to generate the general shape of the impulse response. The models used for the accurate representation of SV parameters such as the dependence of the cluster amplitude and cluster decay rate on the cluster arrival times and Weibull fit for the cluster inter-arrival times are proposed for the first time for the in-vehicle environment.

- We develop small-scale fading characteristics by finding the best fit for the variations of 81 power delay profiles around the average power delay profile. This is the first work to model small-scale fading characteristics within the vehicle.

- We analyze the susceptibility of the channel model parameters to dif-

ferent vehicle types, engine's status and vehicle movement scenarios. Collecting multiple measurement points per transmitter-receiver pair provides parameter values more robust to changes in vehicle types and conditions. Moreover, applying this model to the moving vehicle shows whether the large-scale statistics modeled by removing small-scale fading effects reflect the average behavior of the channel over time and how much of the time variations are the small-scale variations due to scattered propagation paths.

- We propose the simulation model for the UWB channel beneath the chassis based on our findings and give a comparison between the experimental data and the simulation results. The algorithm for generating the channel model and the validation of the generated data with experimental ones has not been done before for the in-vehicle environment.

## 1.5 Organization

The rest of the thesis is organized as follows: Chapter 2 describes the experiment setup and the data processing performed to obtain large-scale and small-scale statistics. Chapter 3 provides the large-scale and small-scale statistics based on channel measurements respectively. In chapter 4, the susceptibility of channel model parameters to different vehicle types and different scenarios is analyzed. Chapter 5 gives the algorithm for the generation of the statistical channel model for IVWSN beneath the chassis and compares the simulation results generated based on our proposed model with experimental

data. Main results are summarized and future work is given in chapter 6.

# Chapter 2

# Experiment Setup and Data Processing

## 2.1 Experiment Setup

The measurements are performed in frequency domain using a vector network analyzer (Agilent VNA 8719ES). We covered a frequency range of 3.1 to 10.6GHz using 1601 points (4.7 MHz between the samples). The UWB antennas used are roughly the size of a playing card and display omnidirectional pattern. The antennas are connected to the VNA via low-loss coaxial cables. The VNA and the cables are calibrated for each frequency band.

The vehicle used for this study is a commercial vehicle, Fiat Linea. The measurements are performed in an empty parking lot. Figure 2.1 shows the locations of one receiver and multiple sensor locations at which the measurements are performed. For each transmitter and receiver pair, impulse response measurements were made at 9 measurement locations arranged in

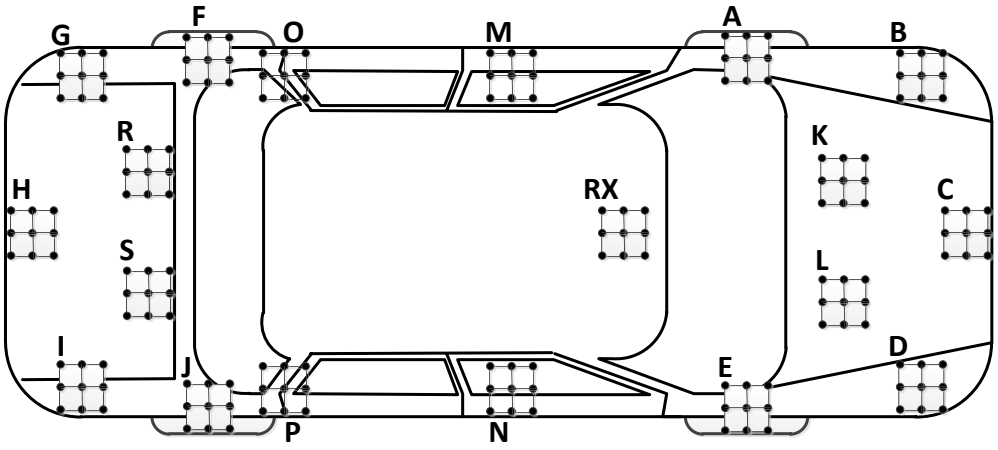


**Figure 2.1:** The locations of one receiver and multiple transmitters used in channel measurements

**Figure 2.2:** Sensor locations arranged in $3 \times 3$ square grid for both transmitter and receiver

a fixed height $3 \times 3$ square grid with 5cm spacing corresponding to half the wavelength at the lowest frequency of interest (3.1GHz) for both transmitter and receiver as shown in Figure 2.2, resulting in 81 measurement points, in order to determine small-scale fading:

The measurement points must be spaced $\lambda_l/2$ or more apart, where $\lambda_l$ is the wavelength at the lower band-edge and equal to 10cm in our case, to allow the measurement points to experience independent fading at all frequencies of measurement. Most indoor measurement campaigns only change the position of the receiver over $7 \times 7$ grid [22, 18, 24] however we couldn't do that in an area small enough that large scale parameters do not change within the confined area of the vehicle thus chose to move both transmitter and receiver locations as would be acceptable [32].

## 2.2 Data Processing

The complex transfer function $H(f)$ obtained from the VNA is processed in Matlab to model both small-scale and large-scale statistics. The frequency response is first weighted by a Hamming window to reduce the sidelobes at the cost of a decrease in measurement resolution. The complex valued impulse response $h(t)$ is then obtained by Inverse Fast Fourier Transform (IFFT). For each of the 81 combinations of transmitter and receiver measurement points, a power delay profile (PDP) is calculated as $|h(t)|^2$, which we call local PDP. All local PDPs are normalized with respect to a reference measurement which is taken at the distance of 1m. The analysis of PDPs follow the same procedure summarized in [14]:

1. The delay axis of the measured multipath profiles for each location is translated by its respective propagation delay. This guarantees that the first bin corresponds to the first multipath component.

2. The delay axis is quantized into bins and the received power is integrated within each bin. The width of the bins are chosen to make a good compromise between high delay resolution and noise reduction. The measurement resolution is approximated by the reciprocal of the bandwidth swept, 0.13ns, multiplied by the additional window function bandwidth. The 6-dB bandwidth of the Hamming window is 1.5 times wider than the rectangular window. The bin width chosen is therefore 0.5ns.

These local PDPs are then averaged over the 81 locations for each transmitter and receiver pair to obtain the small-scale averaged PDP (SSA-PDP). The small-scale statistics are derived by considering the deviations of the 81 local PDPs around the corresponding SSA-PDP whereas the large scale fading is investigated by considering the variation of SSA-PDPs in different areas of the vehicle.

# Chapter 3

# Statistical Channel Modeling

## 3.1 Large-Scale Statistics

The large-scale channel characteristics consist of the path loss with the distance and the general shape of impulse response. These statistics are used in link budget calculation and proper receiver and antenna design together with the small-scale statistics. To have a more accurate large-scale model, we have to remove small-scale variations from our measurements by averaging the measured 81 local PDP to calculate small-scale average PDP's. Since we have 18 measurement locations, we will end up total 18 points to derive desired large-scale statistics.

### 3.1.1 Path Loss Model

Figure 3.1 shows the normalized received power at different frequencies. The normalized received power denotes the magnitude square of the complex transfer function, $|H(f)|^2$, normalized by the total power, $\int_{f_l}^{f_u} |H(f)|^2 df$ where

$f_l = 3.1GHz$ and $f_u = 10.6GHz$, to remove the effect of the distance. The small variation of the normalized received power around the average justifies the common assumption of the independence of the distance-dependence and frequency-dependence of the path loss [15, 33] so allows their separate modeling.

The dependence of the path loss on frequency arises primarily from the antenna power density and gain variation with $f$, and additionally from frequency-selective physical propagation phenomena such as scattering, diffraction, and can be modeled as

$$PL_{[dB]}(f) = PL_{[dB]}(f_0) + 10mlog_{10}(\frac{f}{f_0}) \tag{3.1}$$

where $PL_{[dB]}(f)$ is the path loss at frequency $f$ in decibels, $PL_{[dB]}(f_0)$ is the path loss at reference frequency $f_0$ in decibels and $m$ is the frequency dependent path loss exponent. The cumulative density function of $m$ for different locations is shown in Figure 3.2.

The dependence of the path loss on distance arises primarily from the free-space loss and vehicular environment affecting the degree of refraction, diffraction, reflection and absorption, and can be modeled as

$$PL_{[dB]}(d) = PL_{[dB]}(d_0) + 10nlog_{10}(\frac{d}{d_0}) + Z \tag{3.2}$$

where $PL_{[dB]}(d)$ is the path loss at distance $d$ in decibels, $PL_{[dB]}(d_0)$ is the path loss at reference distance $d_0$ in decibels, $n$ is the distance dependent path loss exponent and $Z$ is a zero-mean Gaussian random variable with standard

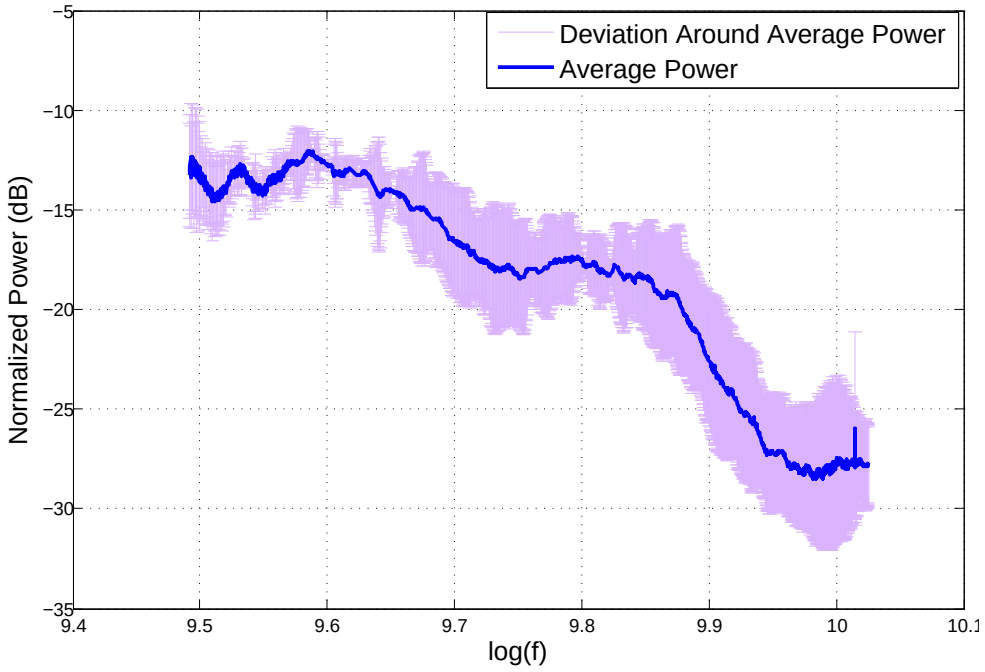


**Figure 3.1:** Normalized received power as a function of frequency.

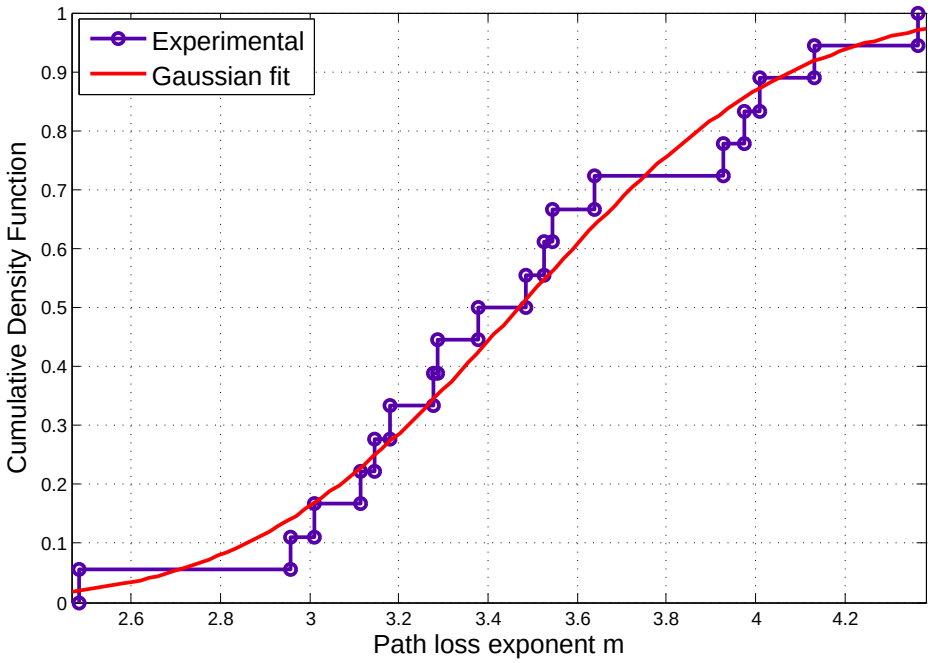


**Figure 3.2:** Cumulative density function of frequency dependent path loss exponent.

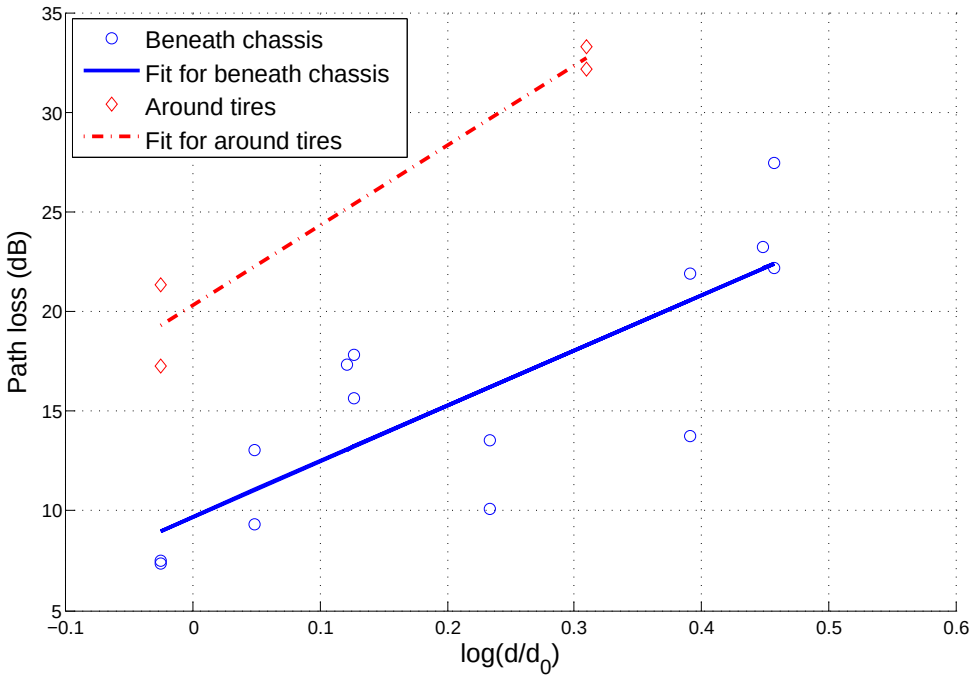


**Figure 3.3:** Path loss as a function of the logarithm of the distance.

deviation $\sigma_z$ representing the random deviations in the model.

Figure 3.3 shows the path loss at different $log_{10}(\frac{d}{d_0})$ for $d_0 = 1$m together with the least square fit curve satisfying Equation 3.2. Since the behavior of the path loss at the tires is very different from the remaining locations beneath the chassis, the distance dependent path loss exponents are estimated separately: $n = 4$ for the tires and $n = 2.8$ beneath the chassis. Compared with free space, $n = 2$, the path loss exponents beneath the chassis of a vehicle is much higher especially at the tires. This exponent is consistent with previous in-vehicle measurements performed beneath the chassis excluding the tire: The exponent $n = 2.8$ found in this paper is between the exponents calculated for the GM Escalade and Ford Taurus being $n = 1.61$ and $n = 4.58$ respectively [10]. Furthermore, the reference path loss $PL_{[dB]}(d_0)$ is much higher for the tire than the remaining locations beneath the chassis due to the higher number of obstructions between the tires and receiver resulting in higher energy absorption.

Figure 3.4 shows the experimental cumulative density function of the power variation denoted by $Z$ in Equation 3.2 together with the least square fit of the cumulative density function of the Gaussian variable. The empirical values for the power variation are calculated by subtracting the mean path loss represented by the best fit in Figure 3.3 from the actual path loss values. The figure demonstrates that the common Gaussian fit is also a good model for beneath the chassis in-vehicle environment with standard deviation $\sigma_z = 3.305$.

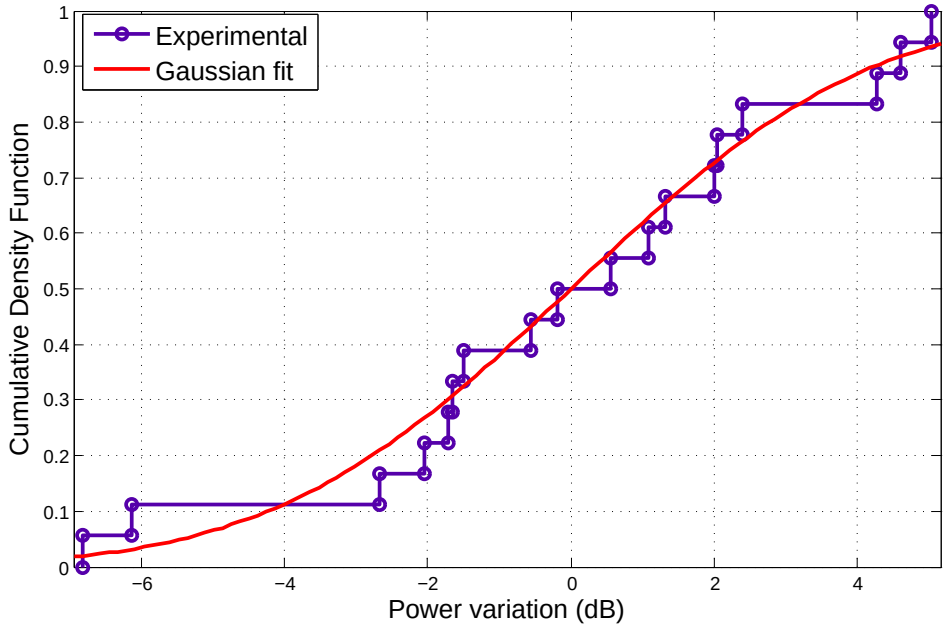


**Figure 3.4:** Cumulative density function of the power variation.

### 3.1.2 General Shape of Impulse Response

The SSA-PDP at different locations beneath the chassis consists of several random clusters. Figures 3.5 and 3.6 show the example SSA-PDPs normalized by the receive energy at reference distance $d_0 = 1m$ for the left front tire (point A) and left rear chassis (point G) respectively.

The random clusters are modeled using the commonly used UWB channel model called Saleh-Valenzuela (SV) model [13]. SV model describes the impulse response as

$$h(t) = \sum_{l=0}^{L} \sum_{k=0}^{K} a_{l,k} e^{j\theta_{l,k}} \sigma(t - T_l - \tau_{l,k}) \tag{3.3}$$

where $a_{l,k}$ and $\theta_{l,k}$ are the gain and phase of the $k$-th component in the $l$-th cluster respectively, $T_l$ is the delay of the $l$th cluster, $\tau_{l,k}$ is the delay of the $k$-th multipath component relative to the $l$-th cluster arrival time $T_l$, $K$ is the number of the multipath components within a cluster and $L$ is the number of clusters. The phases $\theta_{l,k}$ are uniformly distributed in the range $[0, 2\pi]$.

We now analyze the statistics of the decay rate of the cluster amplitudes, the decay rate of the ray amplitudes within each cluster and interarrival times of clusters. Since it was not possible to resolve the inter-path arrival times within each cluster by inverse Fourier transform of the measured data,we do not analyze the ray arrival rates within each cluster. The arrival time and magnitude of individual clusters in each SSA-PDP is calculated by using the automatic clustering algorithm described in [34] and validating the correctness of the algorithm by visual inspection. The automatic clustering algorithm is

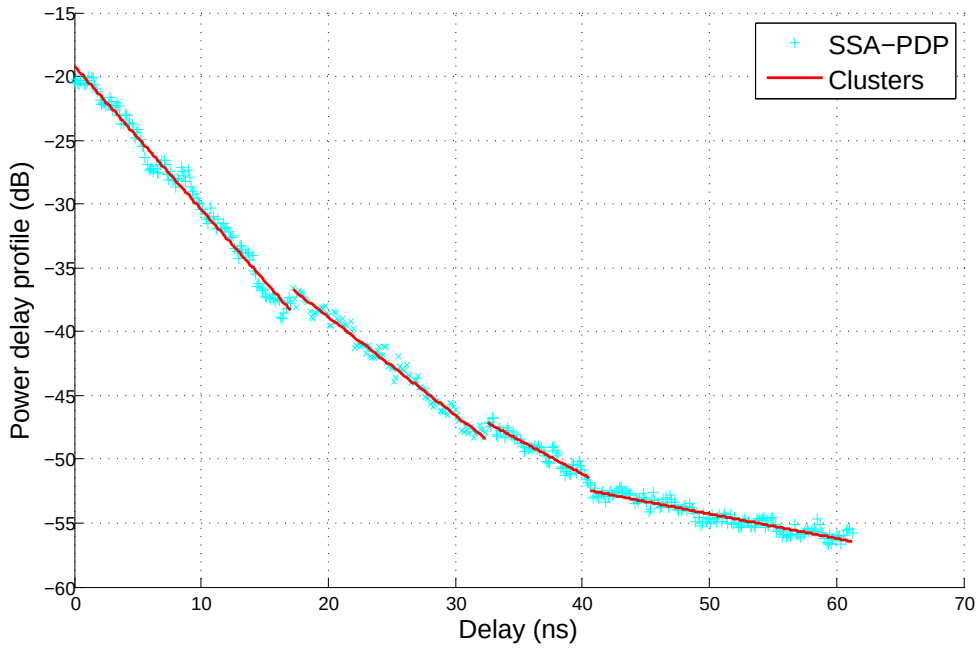


**Figure 3.5:** SSA-PDP for the left front tire (point A).

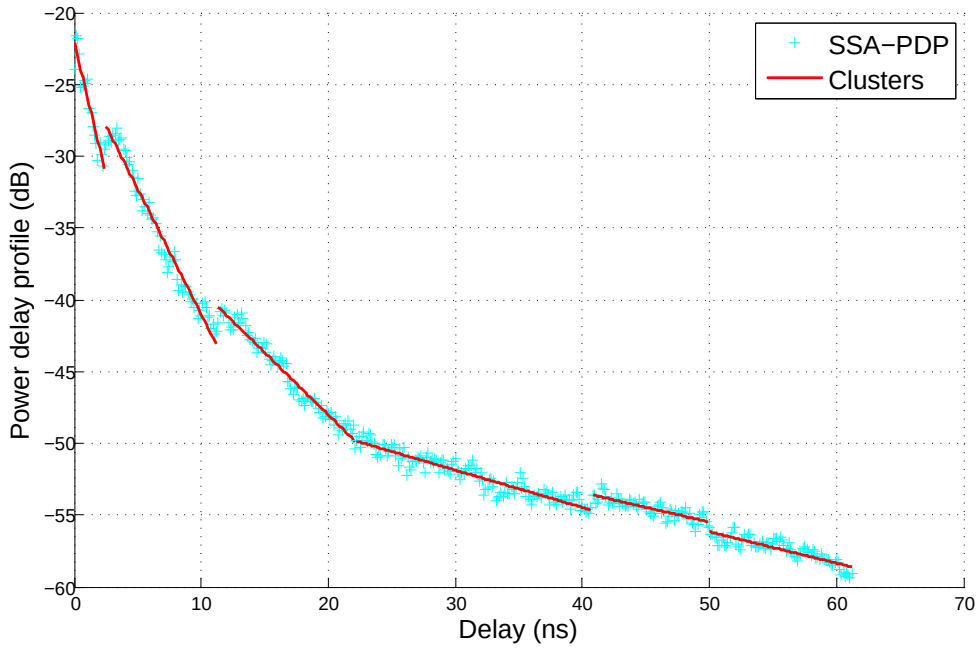


**Figure 3.6:** SSA-PDP for the left rear chassis (point G).

based on identifying the changes in the slope of the impulse response based on the assumption that all changes in slope correspond to the start of a new cluster as illustrated in Figures 3.5 and 3.6.

Figure 3.7 shows the decay rate of the cluster amplitude as a function of the cluster arrival time. The horizontal and vertical axes represent the time of arrival of each cluster and the power of the first bin of each cluster relative to the total energy respectively. We observe that the cluster amplitude decreases at a slower rate after 27ns delay resulting in the following dual slope linear model:

$$f(T_l) = \begin{cases} p_{11} \cdot T_l + p_{10}, T_l \leq b1 \\ p_{21} \cdot T_l + p_{20}, T_l > b1 \end{cases} \tag{3.4}$$

where $f(T_l)$ represents the power of the first bin of the cluster arriving at delay $T_l$ relative to the total energy expressed in decibels, $b_1$ is the delay index for the breakpoint between the two lines, $p_{11}$ and $p_{21}$ are the slopes of the least square fit line before and after the breakpoint respectively, $p_{10}$ and $p_{20}$ are the intercept of the least square fit line before and after the breakpoint respectively.

As illustrated in Figures 3.5 and 3.6, the $k$-th bin of each cluster $l$ has an additional linear decay with respect to the first component of that cluster in decibels formulated as follows:

$$g(T_l + \tau_{l,k}) = f(T_l) - \gamma(T_l)\tau_{l,k} \tag{3.5}$$

where $g(T_l + \tau_{l,k})$ is the power of the $k$-th component of the cluster arriving at delay $T_l$ relative to the total energy expressed in decibels and $\gamma(T_l)$ is the decay

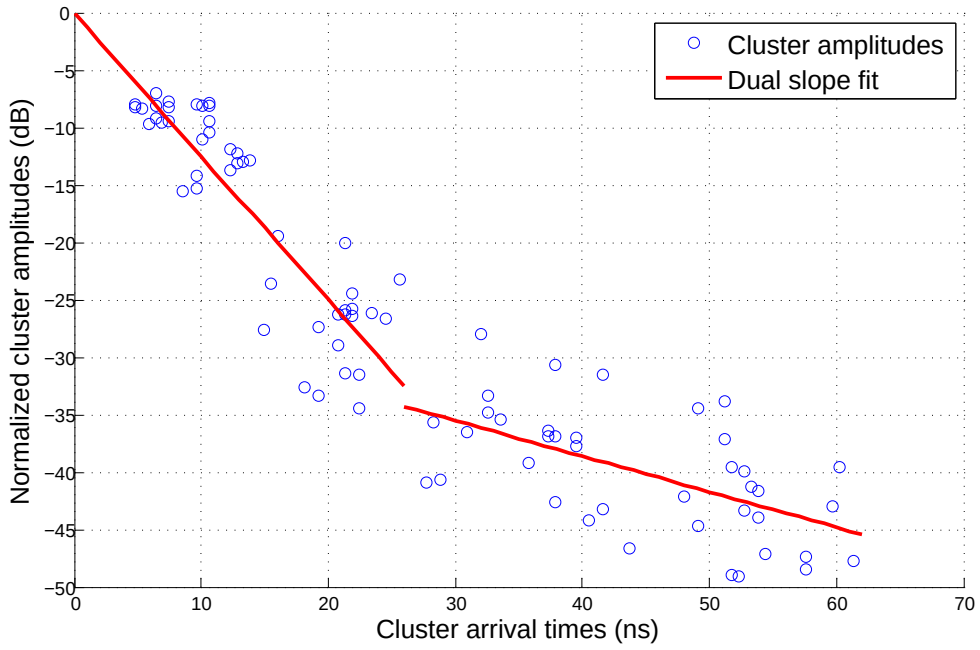


**Figure 3.7:** Normalized cluster amplitudes as a function of cluster arrival time.

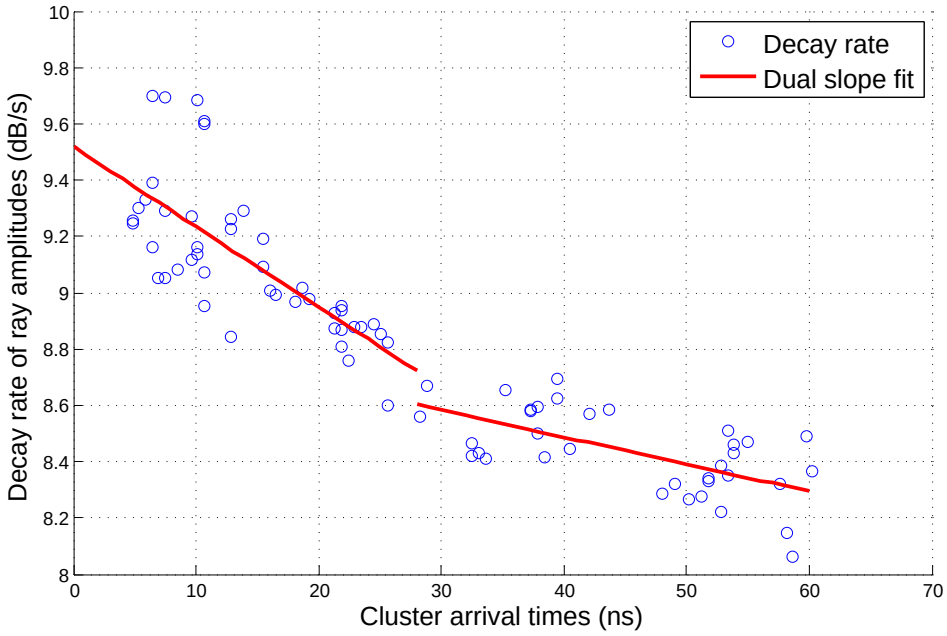


**Figure 3.8:** Ray decay rate as a function of cluster arrival time.

rate as a function of the cluster arrival time $T_l$. Figure 3.8 shows the decay rate $\gamma$ as a function of the cluster arrival time $T_l$ based on the measurements beneath the chassis. We observe that decay rate can be modeled using the following dual slope linear model:

$$\gamma(T_l) = \begin{cases} q_{11} \cdot T_l + q_{10}, T_l \leq b2 \\ q_{21} \cdot T_l + q_{20}, T_l > b2 \end{cases} \tag{3.6}$$

where $b_2$ is the delay index for the breakpoint between the two lines, which is equal to $b_1 = 27ns$ in this case, $q_{11}$ and $q_{21}$ are the slopes of the least square fit line before and after the breakpoint respectively, $q_{10}$ and $q_{20}$ are the intercept of the least square fit line before and after the breakpoint respectively. The dependence of the cluster amplitudes and ray decay rate on the cluster arrival time has not been analyzed before in the literature on beneath the chassis channel models [9, 10, 11].

Figure 3.9 shows the cumulative density function for inter-arrival times of the clusters. The arrival time of the first cluster is the propagation delay, which is a function of the distance between transmitter and receiver, and speed of light. We investigated the interarrival times for the second and third clusters, denoted by $l = 2, 3$, and the remaining clusters, denoted by $l > 3$, separately since they exhibit very different behavior as illustrated in the Figure. The exponential distribution is associated with inter-cluster arrival times in previous beneath the chassis measurements [10, 11]. However, we observe that Weibull distribution provides a better fit to our data. The main reason is expected to be the nonrandomness of the local structure of the

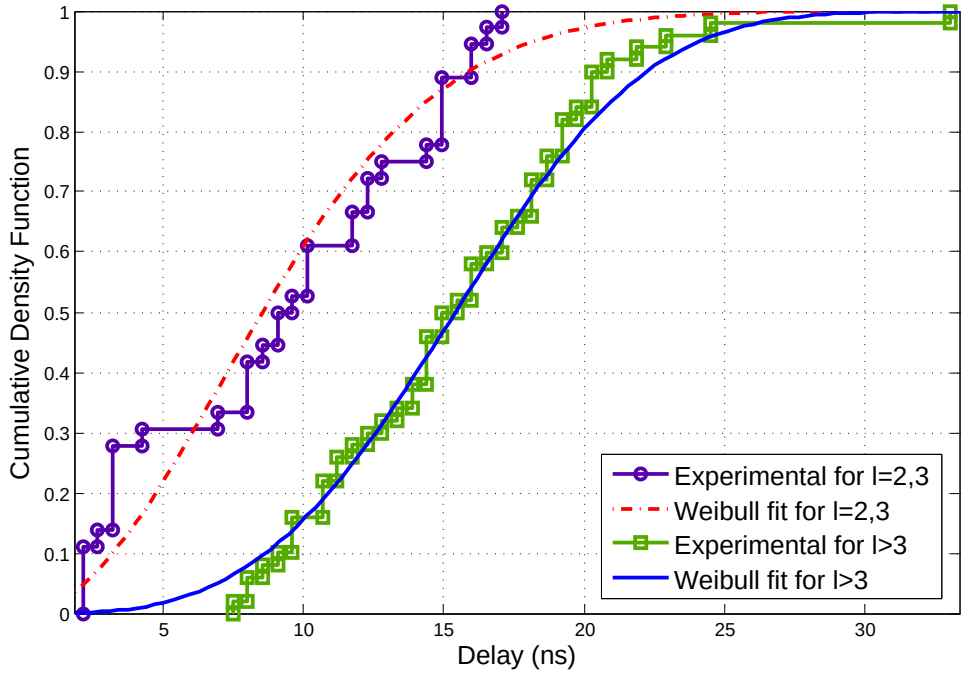


**Figure 3.9:** Cumulative density function of inter-arrival times of the clusters

in-vehicle environment [23]. This result is also validated by using Kolmogorov-Smirnov test which is a nonparametric test for the equality of continuous, one-dimensional probability distributions comparing a sample with a reference probability distribution. Kolmogorov-Smirnov statistics for exponential and Weibull distributions are 0.3124 and 0.1575 respectively. The two parameters of Weibull distribution, i.e. shape parameter and scale parameter, are found to be $\lambda_1 = 10.3ns$ and $k_1 = 1.93$ respectively for $l = 2, 3$, and $\lambda_2 = 17.2ns$ and $k_2 = 3.26$ respectively for the remaining clusters.

## 3.2 Small-Scale Statistics

In the previous chapter we provided the large-scale characteristics of the received signal. To improve our model we should also include small-scale statistics which have always been overlooked in the literature. Small-scale fading is defined as the changes in power delay profile caused by small changes in transmitter and receiver position while environment around them does not change significantly in contrast to large-scale fading that models the changes in received signal when the position of the transmitter or receiver varies over a significant fraction of distance between them and/or environment around them changes. The small-scale statistics with the large-scale statistics are used in proper receiver and antenna design. Especially by utilizing the information about small-scale fading and signal correlations over a small area, we can evaluate the receiver designs, diversity mechanism and the multiple antenna applications more accurately.

Experience shows that at least 50 measurement points per area are required

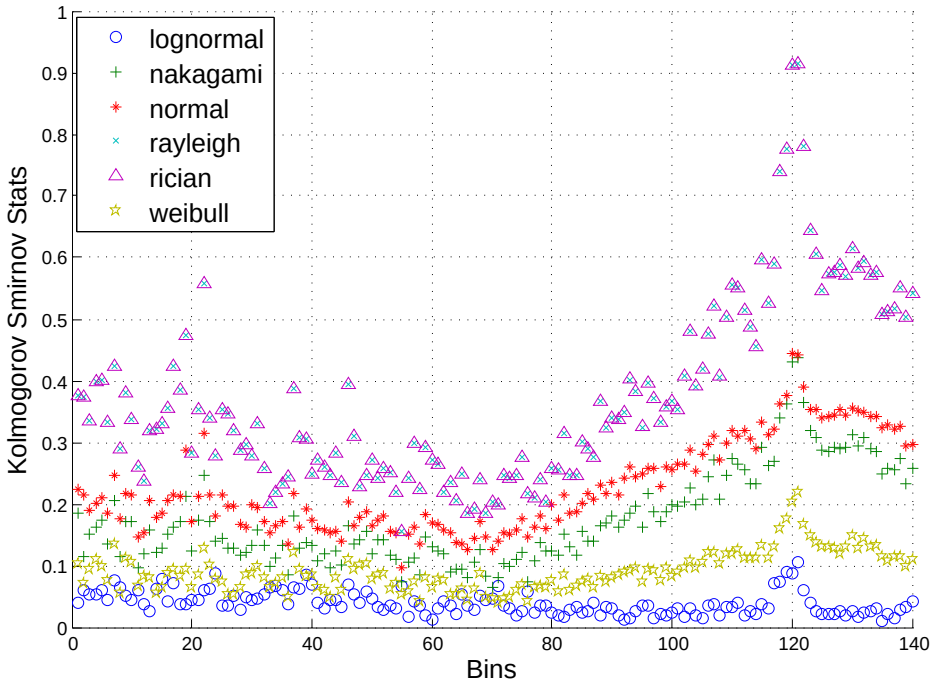


**Figure 3.10:** Kolmogorov Smirnov Test results for the left front tire (point A)

to determine small-scale fading [32]. Since we are not able to place more than 50 points which are separated by $\lambda/2$ neither at the receiver nor the transmitter. Instead, we placed 9 points to each transmitter locations and 9 points to receiver location, namely we measured 81 impulse responses for every transmitter-receiver pair. The small-scale statistics are characterized by fitting 81 amplitude values $|h(t)|$ obtained for each delay bin to many alternative distributions listed in [32], i.e. lognormal, Nakagami, normal, Rayleigh, Rician and Weibull distributions. We compared the fits by using Kolmogorov-Smirnov test. Lognormal distribution is the best model in almost every bin at different sensor locations. Figure 3.10 shows the Kolmogorov-Smirnov test results for the left front tire as an example.

Since the best fit for the variations of $|h(t)|$ at 81 locations is lognormal distribution, the local PDP, i.e. $20log(|h(t)|)$, at each delay bin has a normal distribution with $\mu$ parameter as the value of the SSA-PDP in the corresponding bin and $\sigma$ parameter specifying the variations around the SSA-PDP in decibels. Figure 3.11 shows the values of the $\sigma$ parameter of lognormal distributions for each bin. The $\sigma$ values are mostly concentrated between 3 and 4.2 without any trend of decrease or increase with the increasing delay. We also investigated the dependency of the mean value of the $\sigma$ parameter over all delay bins on the distance. As shown in Figure 3.12, $\sigma$ values do not follow any pattern with respect to distance, so we take $\sigma$ as the average of all points, which is 3.88.

The average correlation coefficient of the small-scale fading between bins at different lags is also calculated. As illustrated in Figure 3.13, the correlation is around 0.2 between adjacent bins and below 0.1 for nonadjacent bins. We

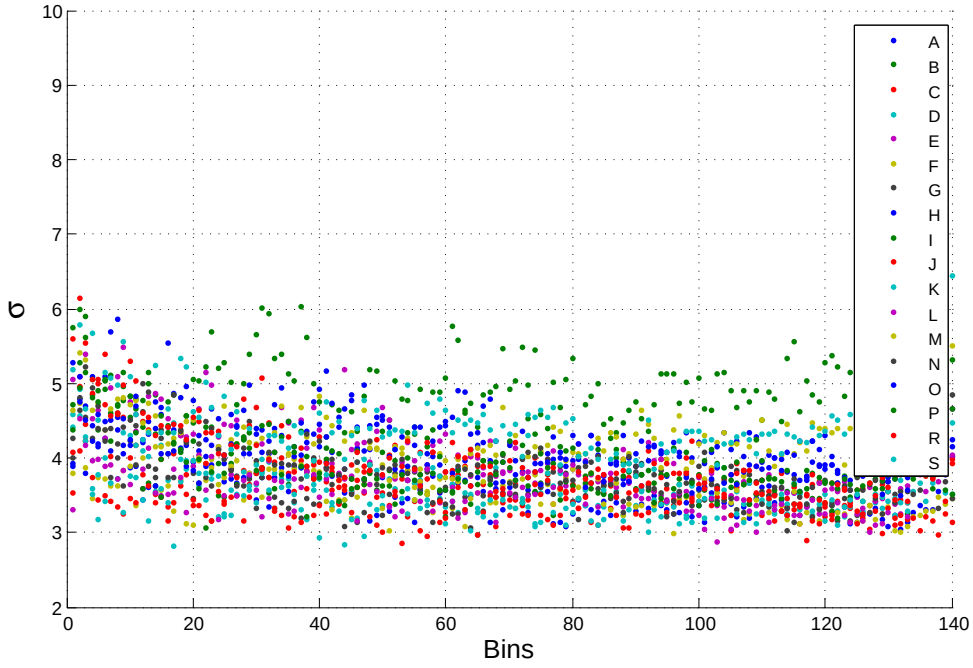


**Figure 3.11:** Values of the $\sigma$ parameter of lognormal distribution at different locations and different bins.

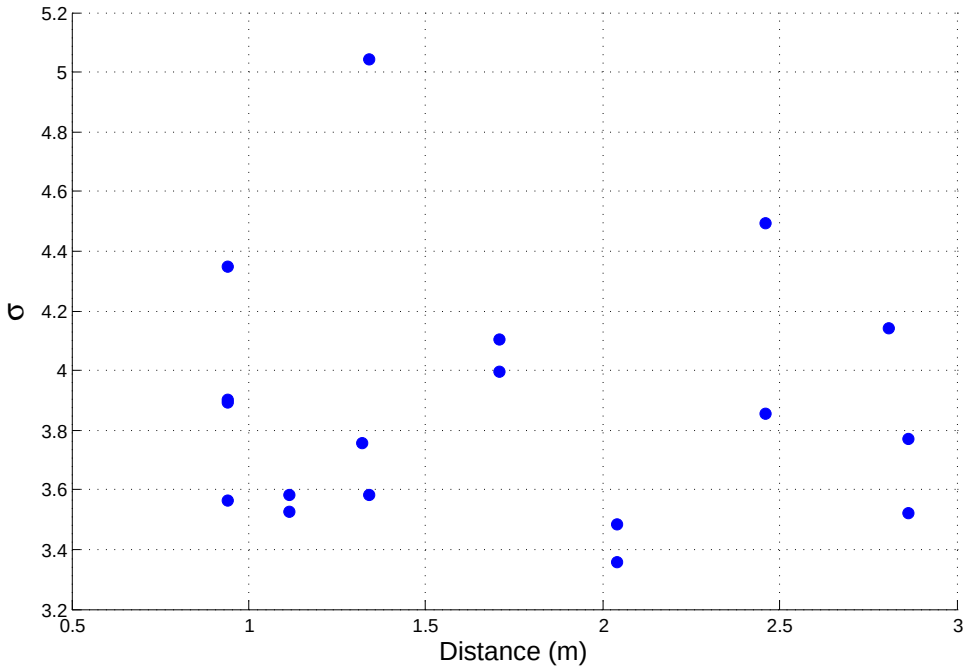


**Figure 3.12:** Mean value of the $\sigma$ parameter of lognormal distribution as a function of distance.

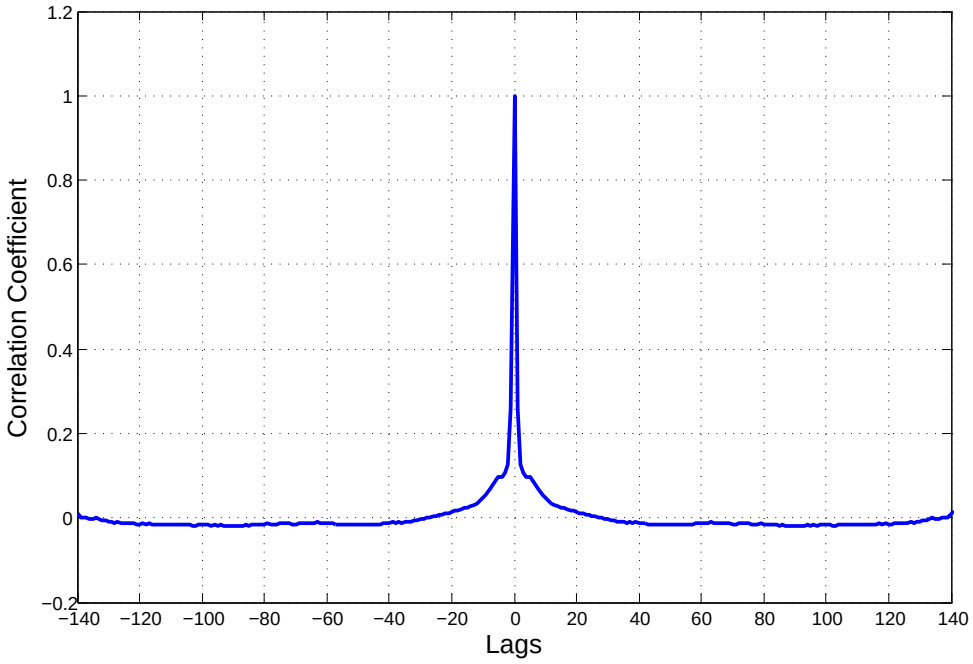


**Figure 3.13:** Average correlation coefficient of the small-scale fading between bins at different lags.

can therefore simplify the model by assuming each bin fades independently.

The small-scale statistics has not been modeled before in the literature on beneath the chassis channel models [9, 10, 11].

# Chapter 4

# Susceptibility of Parameters to Different Scenarios

To validate our findings, we investigated the channel characteristics for different scenarios. First, we analyzed the changes in the channel characteristics when the engine is turned on compared to the engine off scenario. Then we repeated the experiments on a vehicle very different from Fiat Linea, Peugeot Bipper that is a minivan with shorter length, higher chassis and ceiling, to determine the susceptibility of channel parameters to different vehicle types. Finally, we collected the data for the moving vehicle and applied the model to analyze whether the large-scale statistics modeled by removing small-scale fading effects reflect the average behavior of the channel over time and how much of the time variations are the small-scale variations due to scattered propagation paths.

The large-scale and small-scale models derived in Sections 3.1 and 3.2 respectively are summarized in Table 4.1. All the parameters in this table have

been defined before except different distance dependent path loss exponents for chassis and tire, i.e. $n_c$ and $n_t$ respectively, and different path losses at reference distance $d_0$ in decibels, i.e. $PL_c(d_0)$ and $PL_t(d_0)$ respectively. Tables 4.2, 4.3, 4.4, 4.5 and 4.6 summarize the parameters of cluster arrivals, cluster power decay, ray decay rate, path loss and power variation, and small-scale fading respectively for four scenarios: "engine off" is for Fiat Linea engine turned off, "engine on" is for Fiat Linea engine turned on, "Bipper" is for Peugeot Bipper engine turned off, "Moving" is for Fiat Linea driven on the road.

| | |
|---|---|
| | Large Scale Model |
| Cluster Arrival | $T_l - T_{l-1} \sim \begin{cases} W(\lambda_1, k_1), & l = 2, 3 \\ W(\lambda_2, k_2), & l > 3 \end{cases}$ |
| Cluster Decay | $f(T_l) = \begin{cases} p_{11} \cdot T_l + p_{10}, T_l \leq b1 \\ p_{21} \cdot T_l + p_{20}, T_l > b1 \end{cases}$ |
| Ray Decay | $g(T_l + \tau_{l,k}) = f(T_l) - \gamma(T_l)\tau_{l,k}$ |
| | $\gamma(T_l) = \begin{cases} q_{11} \cdot T_l + q_{10}, T_l \leq b2 \\ q_{21} \cdot T_l + q_{20}, T_l > b2 \end{cases}$ |
| Path Loss | $PL(d) = \begin{cases} PL_c(d_0) + 10n_c log_{10}(\frac{d}{d_0}), \text{chassis} \\ PL_t(d_0) + 10n_t log_{10}(\frac{d}{d_0}), \text{tires} \end{cases}$ |
| Power Variation | $Z \sim N(0, \sigma_z^2)$ |
| | Small Scale Model |
| Variation (dB) | $S_n \sim N(0, \sigma^2)$ |

**Table 4.1:** Statistical large-scale and small-scale models

| Scenario | $\lambda_1$ | $k_1$ | $\lambda_2$ | $k_2$ |
|---|---|---|---|---|
| Engine off | 10.3 | 1.93 | 17.2 | 3.26 |
| Engine on | 15.1 | 2.77 | 20.5 | 2.24 |
| Moving | 18.1 | 3.06 | 21.7 | 2.60 |
| Bipper | 12.6 | 2.24 | 19.9 | 2.08 |

**Table 4.2:** Parameters of cluster arrivals. The unit of $\lambda_1$ and $\lambda_2$ is $ns$.

| Scenario | $p_{11}$ | $p_{10}$ | $p_{21}$ | $p_{20}$ | $b_1$ |
|---|---|---|---|---|---|
| Engine off | $-1.24 \cdot 10^9$ | $-0.07$ | $-3.09 \cdot 10^8$ | $-26.25$ | $2.7 \cdot 10^{-8}$ |
| Engine on | $-1.31 \cdot 10^9$ | $-0.27$ | $-3.03 \cdot 10^8$ | $-28.39$ | $2.8 \cdot 10^{-8}$ |
| Moving | $-1.34 \cdot 10^9$ | $-0.31$ | $-2.84 \cdot 10^8$ | $-29$ | $2.6 \cdot 10^{-8}$ |
| Bipper | $-0.88 \cdot 10^9$ | $-7.54$ | $-2.51 \cdot 10^8$ | $-26.4$ | $2.9 \cdot 10^{-8}$ |

**Table 4.3:** Parameters of cluster power decay. The unit of $p_{11}$ and $p_{21}$ is $dB/s$. The unit of $p_{10}$ and $p_{20}$ is $dB$. The unit of $b_1$ is $s$.

| Scenario | $q_{11}$ | $q_{10}$ | $q_{21}$ | $q_{20}$ | $b_2$ |
|---|---|---|---|---|---|
| Engine off | $-2.841 \cdot 10^7$ | 9.518 | $-9.624 \cdot 10^6$ | 8.872 | $2.7 \cdot 10^{-8}$ |
| Engine on | $-2.28 \cdot 10^7$ | 9.359 | $-8.684 \cdot 10^6$ | 8.827 | $2.8 \cdot 10^{-8}$ |
| Moving | $-2.616 \cdot 10^7$ | 9.412 | $-10.21 \cdot 10^6$ | 9.269 | $2.6 \cdot 10^{-8}$ |
| Bipper | $-1.657 \cdot 10^7$ | 9.357 | $-7.93 \cdot 10^6$ | 8.906 | $2.8 \cdot 10^{-8}$ |

**Table 4.4:** Parameters of ray decay rate. The unit of $q_{11}$ and $q_{21}$ is $dB/s^2$. The unit of $q_{10}$ and $q_{20}$ is $dB/s$. The unit of $b_2$ is $s$.

| Scenario | $n_c$ | $n_t$ | $PL_c(d_0)$ | $PL_t(d_0)$ | $\sigma_z$ |
|---|---|---|---|---|---|
| Engine off | 2.77 | 4.00 | 9.72 | 20.34 | 3.30 |
| Engine on | 2.33 | 3.59 | 12.87 | 25.23 | 5.11 |
| Moving | 2.58 | - | 11.09 | - | 5.05 |
| Bipper | 2.88 | 4.21 | 14.37 | 26.83 | 2.27 |

**Table 4.5:** Parameters of path loss and power variation. The unit of $PL_c(d_0)$, $PL_t(d_0)$ and $\sigma_z$ is $dB$.

| Case | mean($\sigma$) | min($\sigma$) | max($\sigma$) |
|---|---|---|---|
| Engine off | 3.8843 | 3.3589 | 5.045 |
| Engine on | 3.8662 | 2.972 | 6.8157 |
| Moving | 3.1977 | 2.4742 | 3.6896 |
| Bipper | 3.8300 | 3.1654 | 4.8713 |

**Table 4.6:** Parameters of small scale fading. The unit of $\sigma$ is $dB$.

## 4.1 Effect of Turning Engine On

We repeated $18 \times 81$ measurements by turning the engine of Fiat Linea on to observe the effect of running engine on the channel parameters. The best fit for the inter-arrival times of the clusters is again Weibull distribution with similar shape and scale parameters as illustrated in Table 4.2. Cluster amplitude and ray decay rates as a function of cluster arrival times are again fitted to the dual slope linear model with break points, slope and intercept values very close to the engine off case as illustrated in Tables 4.3 and 4.4 respectively.

Table 4.5 shows that the path loss exponents for the engine on case is smaller than those for the engine off case. This is mainly due to the decrease in the received power at the locations very close to the engine when the engine is turned on. Since the receiver is closer to the front of the vehicle so the engine, higher path loss at closer locations decreases the slope of the path loss line so the path loss exponent. Besides, the standard deviation of the path loss around the mean value increases from 3.3 to 5.11.

The small-scale characteristics are not significantly affected by the running engine. In both engine on and off cases, lognormal fading is observed. Even though there is a difference in the range of the small-scale variance of bin

powers at different locations, the mean variances are very close being 3.88 and 3.87 for engine off and engine on cases respectively as shown in Table 4.6 .

## 4.2 Effect of Vehicle Type

We collected $18 \times 81$ measurements beneath the chassis of Peugeot Bipper to analyze the effect of vehicle type on the channel parameters. The shape and scale parameters of the best Weibull fit, the breakpoints, slope and intercept values of the dual slope linear models for the cluster amplitude and ray decay rates as a function of cluster arrival times are very similar to those of Fiat Linea as illustrated in Tables 4.2, 4.3 and 4.4.

The path loss exponents for the tire and beneath the chassis in Peugeot Bipper is very close to those for Fiat Linea as illustrated in Table 4.5. The previous in-vehicle measurements reported in [10] showed large variation in path loss exponent from $n = 1.61$ in GM Escalade to $n = 4.58$ in Ford Taurus. The small variation in the path loss exponent from $n_c = 2.77$ in Fiat Linea to $n_c = 2.88$ in Peugeot Bipper in our case demonstrates the robustness of our modeling mainly due to collecting multiple measurements separated far enough from each other while keeping the environment around them the same allowing to remove small-scale fading for a better representation of large-scale characteristics. In addition, the standard deviation of the path loss around the mean value is slightly smaller for Peugeot Bipper mainly because of having less scatterers around the receiver location.

The small-scale fading characteristics is also very similar in Fiat Linea

and Peugeot Bipper: Both the range and mean of the variance are very close as shown in Table 4.6.

## 4.3 Effect of Vehicle Movement

We collected measurements at 14 locations beneath the chassis while we drove the vehicle in the campus at about 30km per hour. We did not collect data from the 4 tire locations since the tire movement was breaking the antenna. When we compare the values of the large-scale parameters listed in Tables 4.2, 4.3, 4.4 and 4.5 for the two scenarios of the Fiat Linea with engine on and Fiat Linea driven on the road, we observe that they are very close to each other proving that the large-scale statistics modeled by averaging out small-scale fading reflect the average behavior of the channel over time. The comparison of the small-scale parameters listed in Table 4.6 on the other hand shows only slightly smaller variance for Fiat Linea driven on the road compared to the Fiat Linea engine on case demonstrating that much of the time variations are the small-scale variations due to scattered propagation paths.

Such a detailed comparison of the small-scale averaged large scale characteristics of the stationary case to the average time domain behavior and small-scale variations to the time variations has not been done before. The analysis of the dependence of the vehicle movement on the beneath the chassis channel parameters in [11] has been primarily performed to compare the channel parameters for 10 transmitter-receiver pairs without averaging and modeling small-scale variations in the stationary and moving scenarios

concluding that the movement of the vehicle leads to only slight changes in the channel models without modeling the amount and pattern of changes quantitatively.

# Chapter 5

# Channel Model Implementation

## 5.1 Generation of Statistical Channel Model

We now describe the algorithm for generating the statistical channel model using the large-scale and small-scale models summarized in Table 4.1 and the values of the parameters listed in Tables 4.2, 4.3, 4.4, 4.5 and 4.6. The inputs to the algorithm are the distance between the transmitter and receiver, denoted by $d$, and whether the transmitter is in the tire area or any of the remaining locations beneath the chassis, denoted by $o$.

Figure 5.1 gives the basic steps in implementing the channel model:

- The algorithm starts by calculating the cluster arrival times. The first cluster arrives at the propagation delay $T_1 = d/c$. The arrival of the following two clusters is calculated by adding inter-cluster arrival times of distribution Weibull$(\lambda_1, k_1)$ to the previous arrival times. The arrival of the following clusters are then computed by adding the inter-arrival times of Weibull$(\lambda_2, k_2)$ distribution to the previous arrival time. The

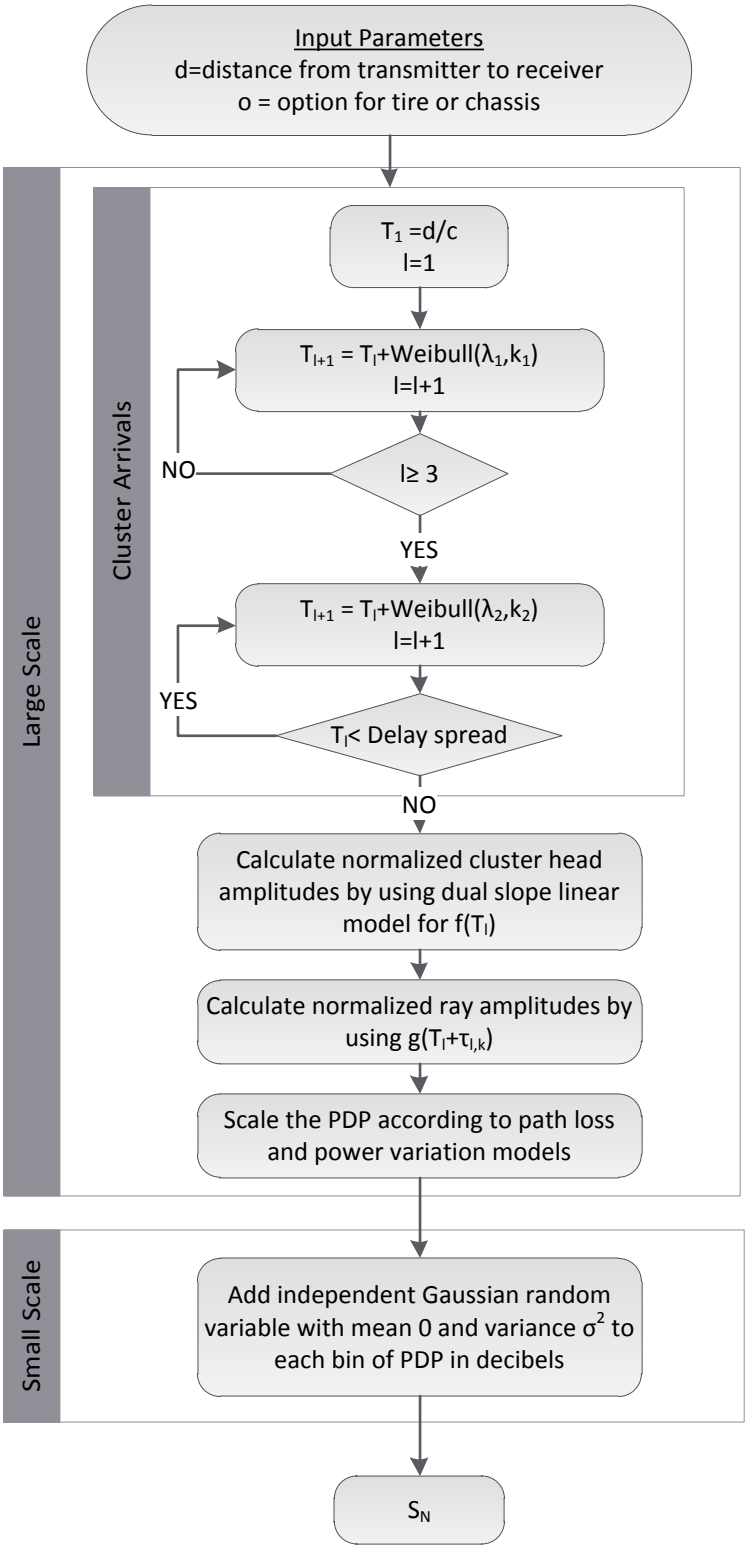


**Figure 5.1:** Flowchart for generating statistical channel model.

cluster arrival times are recorded until the maximum delay spread resulting in the cluster arrival time vector $[T_1, ..., T_M]$.

- The normalized power of the first bin of each cluster $l$ for $l \in [1, M]$ is calculated by using the dual slope linear model $f(T_l)$.

- The normalized power of the $k$-th bin of each cluster $l$ is calculated by using $g(T_l + \tau_{l,k}) = f(T_l) - \gamma(T_l)\tau_{l,k}$ where $\gamma(T_l)$ is computed by using the dual slope linear model.

- The receive power is calculated by inserting the distance parameter $d$ into the corresponding path loss equation depending on whether the location option $o$ is tire or chassis and then adding the Gaussian random variable of mean 0 and variance $\sigma_z^2$ for power variation in decibels. The PDP obtained in the previous step is then normalized by its total power and scaled by the receive power.

- The local PDP is obtained by adding an independent Gaussian random variable of mean 0 and variance $\sigma^2$ to each bin of the SSA-PDP in decibels.

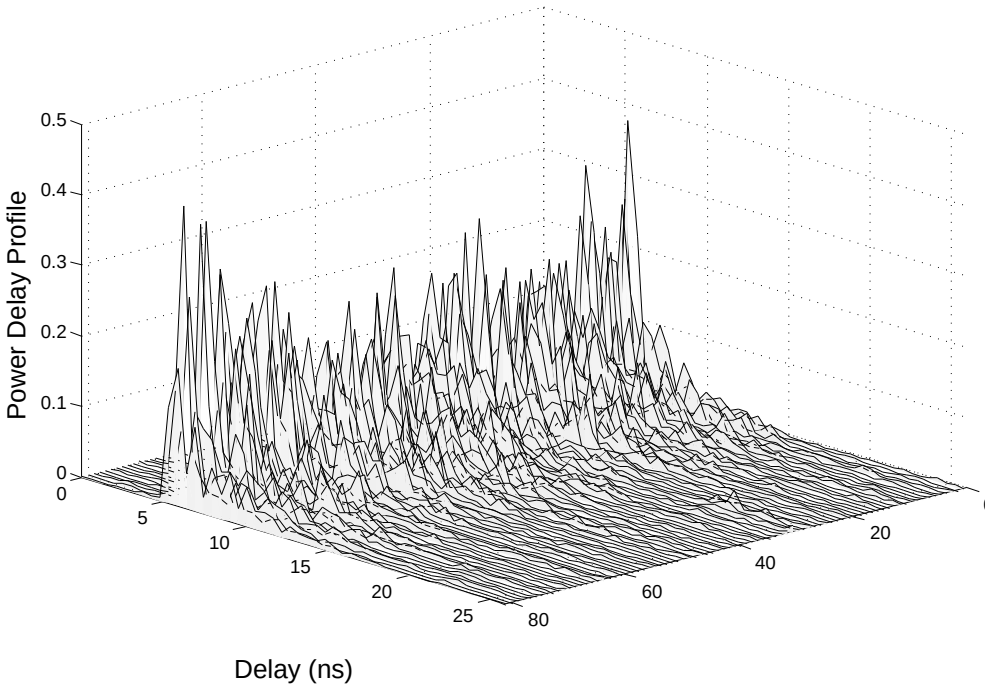


**Figure 5.2:** Experimental local PDPs at the right front chassis (point D).

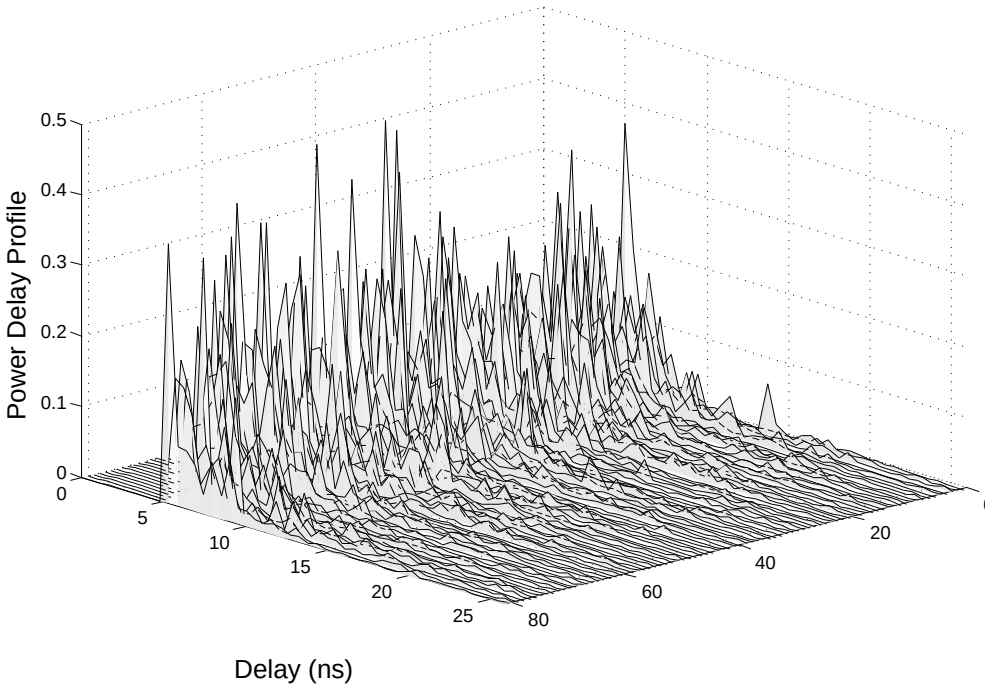


**Figure 5.3:** Simulated local PDPs at the right front chassis (point D).

## 5.2 Simulation Results

We implement the channel model as described in Section 5.1 with the parameters of Fiat Linea engine turned off case listed in Tables 4.2, 4.3, 4.4, 4.5 and 4.6 in MATLAB and compared the results to the experimental data.

Figs. 5.2 and 5.3 show an examplary set of experimental and simulated local PDPs for the right front chassis (point D). Since the comparison is done between statistical realizations, the comparison can be done only qualitatively. It is clear that the measured and simulated local PDPs agree in that sense.

Fig. 5.4 shows the cumulative density function (cdf) of the receive energy for both experimental and simulated 81 local PDPs for the right front chassis (point D). The simulated cdf is slightly narrower than the experimental cdf. The main reason for this behavior is expected to be the slight variation of large-scale statistics such as distance and illumination conditions over the 81 locations in the experimental data.

Fig. 5.5 shows the cdf of the root mean square (rms) delay spread for measured and simulated PDPs over $18 \times 81$ measurement points. The rms delay spread for measured and simulated data are again in close aggrement with means 17.73ns and 17.82ns respectively.

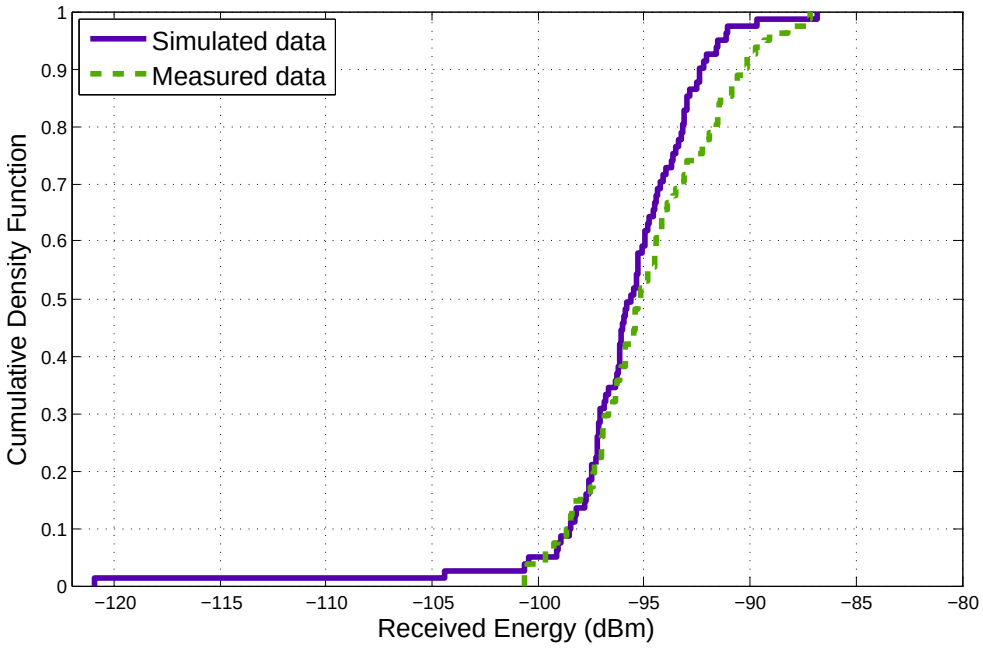


**Figure 5.4:** Cumulative density function of the receive energy of the experimental and simulated 81 local PDPs for the right front chassis (point D).

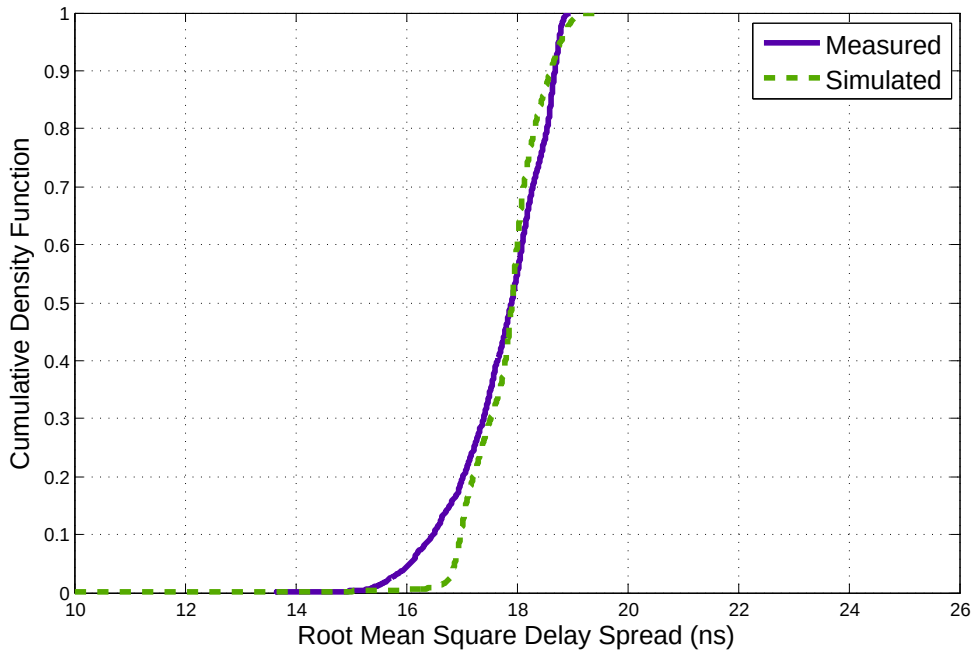


**Figure 5.5:** Cumulative density function of the root mean square delay spread for measured and simulated PDPs over $18 \times 81$ measurement points.

# Chapter 6

# Conclusion

We analyze the small-scale and large-scale statistics of the UWB channel beneath the chassis of the vehicle by collecting data at various sensor locations each of which consists of 81 measurement points corresponding to the transmitters and receivers located on a fixed height $3 \times 3$ square grid with 5cm spacing. Collecting multiple measurements for each transmitter-receiver pair allows us to both improve the accuracy of the large-scale fading representation and model small-scale fading characteristics. The parameters are derived for path loss, power variation around path loss, Saleh-Valenzuela (SV) model and small-scale fading for four different scenarios: Fiat Linea engine off, Fiat Linea engine on, Peugeot Bipper engine off and Fiat Linea driven on the road. Main results of the paper are as follows:

- The distance dependent path loss exponent around the tires and remaining locations beneath the chassis are very different requiring separate models. The power variation around path loss has lognormal distribution justifying the common shadow fading model.

- The clustering phenomenon observed in the power delay profile of all the links is well characterized by SV model. The cluster amplitude and cluster decay rate is formulated as a function of the cluster arrival times using dual slope linear model. Such a model has not been developed before for in-vehicle environment. Moreover, cluster inter-arrival times are modeled using Weibull distribution providing a better fit than the commonly used exponential distribution in the literature due to the non-randomness of the local structure of the in-vehicle environment. Furthermore, a separate Weibull fit is used for the first 3 and the following clusters due to the consistently smaller inter-arrival times obtained for the first 3 clusters.

- The variations of the local power delay profiles around the small-scale averaged power delay profiles in decibels at each delay bin is well modeled by Gaussian distribution with variance independent of the value of the delay and distance between transmitter and receiver. Such an analysis of small-scale fading characteristics has not been done before for the in-vehicle environment.

- Effect of turning the engine on for the same vehicle is investigated for the first time in the literature. Running engine only slightly affected the values of SV and small-scale fading parameters while decreasing the path loss exponents due to the decrease in the received power at the locations very close to the engine.

- Effect of vehicle type on the large-scale and small-scale parameters is found to be very small compared to previous beneath the chassis models

demonstrating the robustness of our modeling approach mainly due to collecting multiple measurements separated far enough from each other while keeping the environment around them the same allowing to remove small-scale fading for a better representation of large-scale characteristics. The path loss exponent only changed from $n_c = 2.77$ in Fiat Linea to $n_c = 2.88$ in Peugeot Bipper in our case whereas the previous in-vehicle measurements reported in [10] showed large variation in path loss exponent from $n = 1.61$ in GM Escalade to $n = 4.58$ in Ford Taurus.

- Effect of moving vehicle on the large-scale and small-scale parameters is found to be very similar to those of the same vehicle with engine turned on demonstrating that the large-scale statistics modeled by averaging out small-scale fading reflect the average behavior of the channel over time and much of the time variations are the small-scale variations due to scattered propagation paths.

- The algorithm for generating the channel model is given. The comparison of the generated power delay profiles with the experimental ones show good agreement validating our model.

In the future, we aim to build models for other parts of the vehicle including engine compartment, passenger compartment, and a more detailed model for the time variations of the power delay profiles.

# References


[1] N. Navet, Y. Song, F. Simonot-Lion, and C. Wilwert, "Trends in automotive communication systems," *Proceedings of the IEEE*, vol. 93, pp. 1204–1223, June 2005.

[2] S. C.Ergen, A. Sangiovanni-Vincentelli, X. Sun, R. Tebano, S. Alalusi, G. Audisio, and M. Sabatini, "The tire as an intelligent sensor," *IEEE Transactions on Computer-Aided Design of Integrated Circuits and Systems*, vol. 28, pp. 941–955, July 2009.

[3] W. Niu, J. Li, S. Liu, and T. Talty, "Intra-vehicle ultra-wideband communication testbed," in *IEEE Milcom*, October 2007, pp. 1–6.

[4] O. Tonguz, H. Tsai, C. Saraydar, T. Talty, and A. Macdonald, "Intra-car wireless sensor networks using rfid: Opportunities and challenges," in *IEEE Mobile Networking for Vehicular Environments*, May 2007, pp. 43–48.

[5] H. Tsai, W. Viriyasitavat, O. Tonguz, , C. Saraydar, T. Talty, and A. Macdonald, "Feasibility of in-car wireless sensor networks: A statistical evaluation," in *IEEE Sensor, Mesh and Ad Hoc Communications and Networks (SECON)*, June 2007, pp. 101–111.

[6] A. Moghimi, H. Tsai, C. Saraydar, and O. Tonguz, "Characterizing intra-car wireless channels," *IEEE Transactions on Vehicular Technology*, vol. 58, pp. 5299–5305, November 2009.

[7] M. Ahmed, C.U.Saraydar, T. Elbatt, J. Yin, T. Talty, and M. Ames, "Intra-vehicular wireless networks," in *IEEE Globecom*, November 2007, pp. 1–9.

[8] H. Tsai, O. Tonguz, C. Saraydar, T. Talty, M. Ames, and A. Macdonald, "Zigbee-based intra-car wireless sensor networks: A case study," *IEEE Wireless Communications*, vol. 14, pp. 67–77, December 2007.

[9] W. Niu, J. Li, and T. Talty, "Intra-vehicle uwb channel measurements and statistical analysis," in *IEEE Globecom*, December 2008, pp. 1–5.

[10] ——, "Ultra-wideband channel modeling for intravehicle environment," *EURASIP Journal on Wireless Communications and Networking - Special issue on wireless access in vehicular environments*, pp. 1–12, January 2009.

[11] ——, "Intra-vehicle uwb channels in moving and stationary scenarios," in *IEEE Milcom*, October 2009, pp. 1–6.

[12] J. Reed, *Introduction to ultra wideband communication systems, an*, 1st ed. Upper Saddle River, NJ, USA: Prentice Hall Press, 2005.

[13] A. Saleh and R. A. Valenzuela, "A statistical model for indoor multipath propagation," *IEEE Journal on Selected Areas in Communications*, vol. 5, pp. 128–137, February 1987.

[14] D. Cassioli, M. Z. Win, and A. F. Molisch, "The ultra-wide bandwidth indoor channel: From statistical model to simulations," *IEEE Journal on Selected Areas in Communications*, vol. 20, pp. 1247–1257, August 2002.

[15] B. M. Donlan, D. R. McKinstry, and R. M. Buehrer, "The uwb indoor channel: Large and small scale modeling," *IEEE Transactions on Wireless Communications*, vol. 5, pp. 2863–2873, October 2006.

[16] S. S. Ghassemzadeh, R. Jana, C. W. Rice, W. Turin, and V. Tarokh, "Measurement and modeling of an ultra-wide bandwidth indoor channel," *IEEE Transactions on Communications*, vol. 52, pp. 1786–1796, October 2004.

[17] S. S. Ghassemzadeh, L. J. Greenstein, T. Sveinsson, A. Kavcic, and V. Tarokh, "Uwb delay profile models for residential and commercial indoor environments," *IEEE Transactions on Vehicular Technology*, vol. 54, pp. 1235–1244, July 2005.

[18] J. Lee, "Uwb channel modeling in roadway and indoor parking environments," *IEEE Transactions on Vehicular Technology*, vol. 59, pp. 3171–3180, September 2010.

[19] A. F. Molisch, D. Cassioli, C.-C. Chong, S. Emami, A. Fort, B. Kannan, J. Karedal, J. Kunisch, K. Siwiak, and M. Z.Win, "A comprehensive standardized model for ultrawideband propagation channels," *IEEE*

*Transactions on Antennas and Propagation*, vol. 54, pp. 3151–3166, November 2006.

[20] C. W. Kim, X. Sun, L. C. Chiam, B. Kannan, F. P. S. Chin, and H. K. Garg, "Characterization of ultra-wideband channels for outdoor office environment," in *IEEE Wireless Communications and Networking Conference (WCNC)*, March 2005, pp. 950–955.

[21] C. F. Souza and J. C. R. D. Bello, "Uwb signals transmission in outdoor environments for emergency communications," in *IEEE Computational Science and Engineering Workshop*, July 2008, pp. 343–348.

[22] Y. Chen, J. Teo, J. . Y. Lai, E. Gunawan, K. S. Low, C. B. Soh, and P. B. Rapajic, "Cooperative communications in ultra-wideband wireless body area networks: Channel modeling and system diversity analysis," *IEEE Journal on Selected Areas in Communications*, vol. 27, pp. 5–16, January 2009.

[23] A. Fort, J. Ryckaert, C. Desset, P. Doncker, P. Wambacq, and L. Biesen, "Ultra-wideband channel model for communication around the human body," *IEEE Journal on Selected Areas in Communications*, vol. 24, pp. 927–933, April 2006.

[24] J. Karedal, S. Wyne, P. Almers, F. Tufvesson, and A. F. Molisch, "A measurement-based statistical model for industrial ultra-wideband channels," *IEEE Transactions on Wireless Communications*, vol. 6, pp. 3028–3037, August 2007.

[25] J. Foerster, "Channel modeling sub-committee report final," in *IEEE P802.15-02/490r1-SG3a*, February 2003.

[26] A. F. Molisch, K. Balakrishnan, C. C. Chong, S. Emami, A. Fort, J. Karedal, J. Kunisch, H. Schantz, U. Schuster, and K. Siwiak, "Ieee 802.15.4a channel modelfinal report," in *IEEE 802.15-04-0662-00-004a*, November 2004.

[27] P. C. Richardson, W. Xiang, and W. Stark, "Modeling of ultra-wideband channels within vehicles," *IEEE Journal on Selected Areas in Communications*, vol. 24, pp. 906–912, April 2006.

[28] T. Tsuboil, J. Yamada, N. Yamauchi, M. Nakagawa, and T. Maruyama, "Uwb radio propagation inside vehicle environments," in *International Conference on Intelligent Transportation Systems*, June 2007, pp. 1–5.

[29] I. G. Zuazola, J. Elmirghani, and J. Batchelor, "High-speed ultra-wide band in-car wireless channel measurements," *IET Communications*, vol. 3, pp. 1115–1123, July 2009.

[30] M. Schack, J. Jemai, R. Piesiewicz, R. Geise, I. Schmidt, and T. Kurner, "Measurements and analysis of an in-car uwb channel," in *IEEE Vehicular Technology Conference (VTC)*, May 2008, pp. 459–463.

[31] W. Xiang, "A vehicular ultra-wideband channel model for future wireless intra-vehicle communications (ivc) systems," in *IEEE Vehicular Technology Conference (VTC)*, September 2007, pp. 2159–2163.

[32] A. F. Molisch, "Ultrawideband propagation channels-theory, measurement, and modeling," *IEEE Transactions on Vehicular Technology*, vol. 54, pp. 1528–1545, September 2005.

[33] ——, "Ultra-wide-band propagation channels," *Proceedings of the IEEE*, vol. 97, pp. 353–371, February 2009.

[34] M. Corrigan, A. Walton, W. Niu, J. Li, and T. Talty, "Automatic uwb clusters identification," in *IEEE Radio and Wireless Symposium (RWS)*, January 2009, pp. 376–379.